Available online at www.sciencedirect.com

ScienceDirect

Journal of Volcanology and Geothermal Research 160 (2007) 195–209

Journal of volcanology and geothermal research

www.elsevier.com/locate/jvolgeores

Mechanisms for rainfall-concurrent lava dome collapses at Soufrière Hills Volcano, 2000–2002

Joshua Taron [a,*], Derek Elsworth [a], Glenn Thompson [b], Barry Voight [a]

[a] *College of Earth and Mineral Sciences, Pennsylvania State University, University Park, Pennsylvania 16802-5000, USA*
[b] *British Geological Survey, Keyworth, UK*

Received 8 September 2005; received in revised form 29 September 2006; accepted 4 October 2006

Abstract

The evolution of rainfall-concurrent dome collapses at Soufrière Hills volcano is followed using a limit equilibrium model for rain infiltration into a hot lava carapace. Magma infusing into the dome both supplies heat and builds the slopes. The dome rocks are cooled by episodic rain infiltration and climatic cooling. Rainfall infiltrates fractures that develop in the hot dome carapace, occludes the void space, and staunches effusive gas flow. Gases may originate from juvenile de-gassing of the dome interior, or result from the vaporization of infiltrating water. Gas pressures build in cracks blocked-off by rain, and may destabilize the dome. The effects of dome growth, heating by magma infusion, and cooling by rain infiltration and climatic influences, are combined to follow the growth of the dome towards ultimate collapse. For a fixed suite of strength and transport parameters, and for measured magma influx rates, the evolution of instability may be followed. The evolving factor of safety tracks the observed March 2000 and July 2001 rainfall-concurrent collapse events, which evolve over months. However, the resolution of the hindcast is unable to discriminate between the effects of closely-timed rainfall events (order of hours). The heightening of the dome is shown to exert the principal influence on average slopes and in the evolution of instability. Collapse removes the over-heightened dome, and temporarily restores stability.

Keywords: dome collapse; pyroclastic flows; volcano hazards; rainfall

---

1. Background

Lava dome collapse represents an important and potentially hazardous feature in the life cycle of silicic volcanoes (Miller, 1994). Collapse of the highly gas-charged dome materials may spawn hazardous and highly mobile pyroclastic flows (Nakada and Fujii, 1993; Abdurachman et al., 2000), which can potentially remove greater than 90% of the dome structure, and involve tens of millions of cubic meters of hot tephra.

Recent dome-building activity observed at Soufrière Hills Volcano (SHV), Montserrat has significantly illuminated the mechanisms of dome growth and collapse (Sparks et al., 1998; Watts et al., 2002; Calder et al., 2002; Norton et al., 2002; Carn et al., 2004). Collapses have resulted from the complementary and potentially additive effects of dome oversteepening (Fink and Griffiths, 1998; Sparks et al., 2000) and interior gas-pressurization (Voight

---

* Corresponding author. Fax: +1 814 865 3248.
E-mail addresses: jmt269@psu.edu (J. Taron), elswoth@psu.edu (D. Elsworth), gto@bgs.ac.uk (G. Thompson), voight@ems.psu.edu (B. Voight).

0377-0273/$ - see front matter © 2006 Elsevier B.V. All rights reserved.
doi:10.1016/j.jvolgeores.2006.10.003

and Elsworth, 2000; Elsworth and Voight, 2001). Such collapse modes adequately match observed near-dome tilt (Watson et al., 2000; Widiwijayanti et al., 2005), RSAM (Miller et al., 1998), and gas discharge histories that span major dome collapse events.

However, collapses that occurred during periods of “residual volcanic activity”, 3 July 1998, and those that lacked short-term precursory seismic signals, 20 March 2000 and 29–30 July 2001 (Carn et al., 2004), cannot be explained by slope oversteepening or traditional mechanisms of gas overpressurization. While largely characterized by a deficiency in traditional pre-collapse triggers, these events have directly coincided with periods of intense precipitation (Matthews et al., 2002; Norton et al., 2002; Herd et al., 2003; Matthews and Barclay, 2004; Elsworth et al., 2004; Carn et al., 2004). In the following, we utilize well documented rainfall, seismic, and morphological data for SHV to quantify the role of rainfall as a potential collapse trigger and directly apply a thermal-hydrologic model to the evolution of SHV over the period of January 2000 to October 2002.

2. Rainfall related collapses of the Soufrière Hills Volcano dome

In common with other volcanoes, including Mount St. Helens (Mastin, 1994), Merapi (Voight et al., 2000), and Unzen (Yamasato et al., 1998), a number of large dome collapses at SHV were associated with heavy rainfalls (Matthews et al., 2002; Matthews and Barclay, 2004; Elsworth et al., 2004). This study will focus on the 20 March 2000 and 29–30 July 2001 events, each of which interrupted a period of active dome growth, exhibited an absence of elevated precursory seismic activity, and proceeded concurrently with an intense rainfall event, with retrogressive collapses initiated in the latter stages of heavy rainfall.

By mid March 2000, andesitic growth within the July 1998 collapse scar had reached $\sim 29\times10^6$ m^3 of which $\sim 28\times10^6$ m^3 ($\sim$95%) was removed through numerous pyroclastic flows over a period of $\sim$5 h on 20 March 2000 (Carn et al., 2004). The July 2001 collapse was similar in form, but accumulated a total collapse volume of $\sim 45\times10^6$ m^3 (Carn et al., 2004), or approximately 50% of active dome volume (utilizing unpublished data from the Montserrat Volcano Observatory (MVO) to interpolate extrusion rates from measured active dome volumes on 8 December 2000 and 23 September 2001). Real-time rainfall and seismic data for the July collapse indicate a corresponding and drastic increase in rockfall-type seismic activity (used as a proxy for the evolving instability of the dome) as rainfall approached its maximum intensity of 50 mm in 2 h (e.g. Fig. 2 of Elsworth et al., 2004).

3. Rainfall-related collapse mechanisms

Mechanisms of rainfall induced dome failure, including rainfall-induced erosion of the toe and piping failure in granular materials, may contribute to collapse, but neither mechanism can explain why smaller domes may fail catastrophically, while a larger dome may fail quietly without transecting the dome core. For the smaller, and intrinsically more stable, dome to fail along a deeply transecting surface, some environmental agent such as gas overpressure must act to reduce the strength within the dome core (Elsworth et al., 2004). Alternatively, the presence of an underlying weak seam of overridden rock talus may induce failure, with larger failure resulting if oversteepened slopes cannot be supported, but again, such a collapse is unlikely to reach the core of the dome, barring the contribution of interior fluid pressure (Voight and Elsworth, 2000). Also of interest is the propensity for surface fractures to extend into the dome core by cooling propagation, thereby suddenly releasing trapped overpressures that may destabilize the dome (Mastin, 1994), or contribute to gravitational failure via degradation in strength of the fractured mass (e.g. Mastin, 1994; Elsworth et al., 2004). However, the scale of failures observed on SHV will likely require some additional contribution in the elevation of interior gas pressures (Elsworth et al., 2004). Additionally, cooling of the outer carapace and its effect on deep fracture network structure and propagation remains uncertain and has yet to be quantified. Nonetheless, such a predictor should not be excluded from consideration.

Importantly, contributions from various rainfall induced mechanisms will likely influence a collapse event, and our method is intended to target the most influential. For instance, low-energy lahar-type seismic signals were detected prior to a marked increase in pyroclastic flows for the July 2001 collapse (Carn et al., 2004), indicating possible toe erosion. Again, however, we contend that sustained interior pressures are required to explain transection of the dome core observed in the 1998, 2000, and 2001 events, and propose that rainfall staunching of interior pressures is a principal agent that causatively links these collapses with the high intensity precipitation event.

To explore this causative link, we will quantify the gas pressure-augmenting forces that result from thermal-hydrologic controlled water infiltration into the fractured SHV carapace. Development of a saturated rind staunches gas escape, elevates core pressures, and simultaneously increases destabilizing forces and reduces basal shear strength acting on a failing dome block. This mechanism has been previously explored for exogenous dome growth (Simmons et al., 2003), such as those on Merapi and Unzen, and for the endogenous dominated SHV (Elsworth et al., 2004) to establish feasibility as a failure mechanism. In the following we examine the role of rainfall-triggering of collapse over an extended period of dome growth and collapse (i.e. the phase II dome — November 1999 to present), including the anticipated evolution in dome volume and temperature, whilst considering all contributing factors, over the same extended period. Constraining the model are periodic photogrammetric measurements of dome volume and daily records of rainfall; and the results are compared to monitored RSAM activity and observed collapses.

3.1. Failure mechanism

The first step is to define the magnitude of gas pressures that may develop within the dome. If the dome and its rubble substrate are either sufficiently cool (<100 °C), or a deluge event is of sufficient volume to quench the contacting rock, infiltrating rainwater may saturate the rind and occlude fracture porosity. The infiltration of rainwater, and its vaporization by dome rocks heated by the infusion of magma, may then pressurize fluid within the fracture. If this volume expansion is constrained, the resulting pressures may readily exceed the local strength of the dome rocks (Matthews and Barclay, 2004). However, for non-instantaneous expansion, this induced pressure will be of lower magnitude and be limited to a maximum defined by the thickness of the fluid-saturated rind (the rind hydrostat (Fig. 1b)), and the excess gas overpressure required to inject gas into the rind of water. In comparison with the other pressures involved, this fluid displacement pressure is likely to be small, and is neglected in the analysis. Its inclusion would further elevate the maximum gas overpressure which could be sustained beneath this saturated rind. Overpressurization of the interior may deepen the failure surface under transient (Voight and Elsworth, 2000), or harmonic gas-pressurization (Elsworth and Voight, 2001) (Fig. 1c).

3.2. Determinants of infiltration

To determine whether the proposed mechanism may significantly contribute to instability, we examine the anticipated magnitudes of the pressure-augmenting effects that may result using appropriate physical models and parameters representative of the Soufrière Hills volcano. Maximum overpressures beneath the saturated rind are largely conditioned by whether the thermal and hydraulic state of the dome carapace will allow significant rain infiltration, to what depth this infiltration may penetrate, and whether it is sufficiently rapid to produce destabilization concurrent with the rainfall event.

3.2.1. Hydraulic controls

Hydraulic behavior is controlled by the transport, fluid storage, and immiscible displacement properties of the dome rocks, and may be conveniently indexed relative to permeability defined at the scale of the dome. Although unmeasured, dome-scale permeabilities may be reckoned from tiltmeter-derived estimates of interior gas-pressurization (Widiwijayanti et al., 2005), and COSPEC recorded SO_2 fluxes. An average measured SO_2 flux of 400 tonnes/day (Norton et al., 2002) and 25,000 tonnes/day of steam (Hammouya et al., 1998), driven from the 200 m high July 1998 Soufrière Hills dome by interior conduit overpressures in the range of 0.1 to 5 MPa, results in permeability estimates of the order 10^{-12} to 10^{-9} m^2. Hydraulic constraints developed from this basis (Elsworth et al., 2004) permit depth penetrations concurrent with the rainfall event of 100 m, absent any counteracting thermal restrictions.

The ability of infiltrating rainwater to staunch gas escape will be limited by the hydrostatic pressure of the connected water column and the gas entry (fluid displacement) pressure, p_b, for a total pressure limitation of $p = \rho_W \boldsymbol{g} h + p_b$, for penetration depth, h, water density, ρ_W, and the gravity vector, $\boldsymbol{g}$. Where this gas pressure is exceeded, interior overpressures will be partially released through venting. The gas entry pressure may be reasonably approximated through permeability, k, fracture porosity, n, and interfacial tension between air and water, σ, as $p_b = 0.3\sigma\sqrt{n/k}$ (Leverett, 1941). An idealized, uniform fracture aperture, b, may be linked to permeability as $K = \frac{b^2}{6}\frac{b}{s}$ (e.g. Ouyang and Elsworth, 1993) and porosity as $n = 3b/s$. At the lower bound permeability of 10^{-12} m^2, a small fracture spacing of 1 m, and interfacial tension at the base of the water column (approximating 100 °C) of 58.9×10^{-3} N/m (Lide, 2003), the gas entry pressure, represented as an equivalent static water column head, may thus approach a maximum limitation of 0.1 m. This value is small in comparison to the expected dome infiltration depths, on the order of 60 m, and so may be neglected. Consequently, we select the hydrostatic pressure, representative of a static column of water, as the most conservative evaluation of the maximum excess gas pressure at the base of the saturated rind. Excess gas pressures may

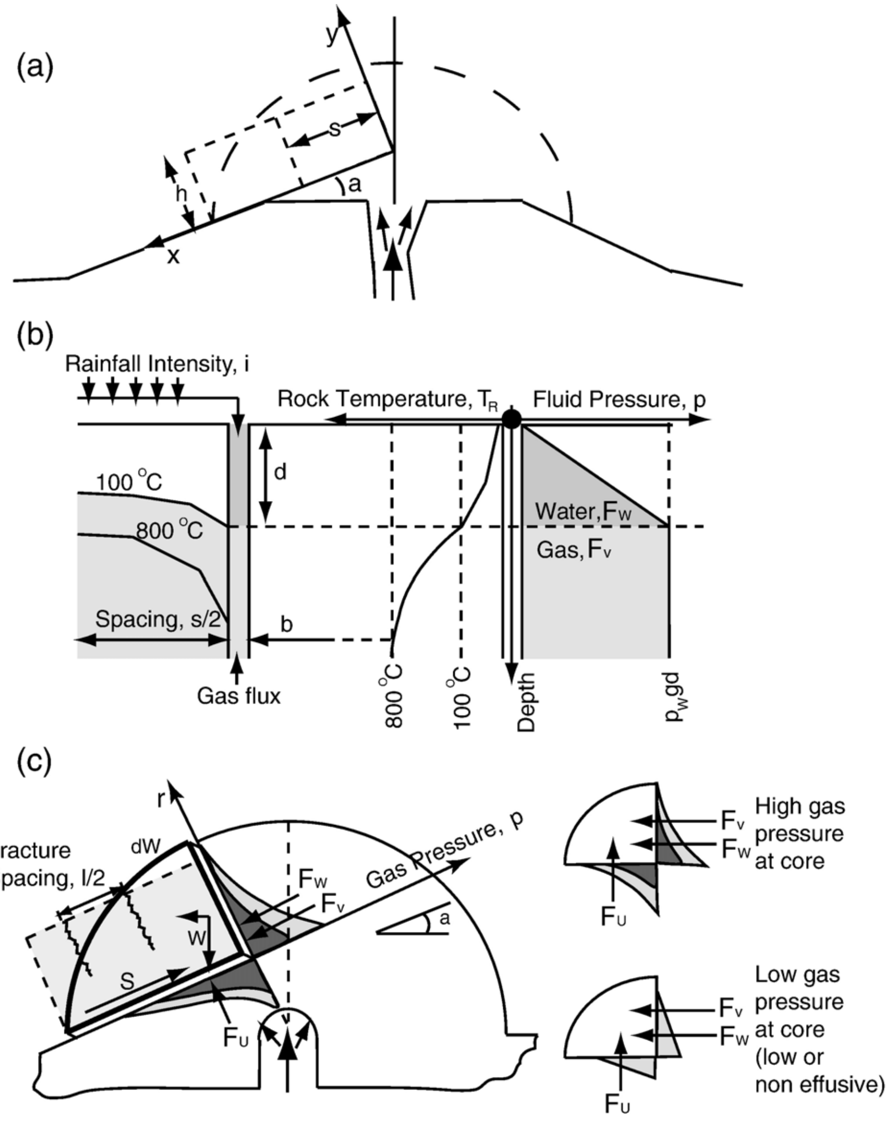

Fig. 1. (Adapted from Elsworth et al., 2004) Schematics of dome geometry, infiltration into carapace, and stability analysis. (a) Insets show locations of (b) and (c). (b) Infiltrating water penetrates fractures to depth, d, enabled by locally depressed 100 °C isotherm, and builds water pressure to $p=\rho_W \boldsymbol{g} d$ at infiltration front. (c) Geometrically separated failure block of weight W raised at angle α to shear plane, held by shear resistance S. Existing gas pressures (dark shading) are augmented (light shading) by stanched gas flow, increasing weakening vapor and water pressure forces (F_V and F_W, respectively) and vapor uplift force (F_U).

indeed exceed this magnitude by a small amount, although this excess is insignificant.

3.2.2. Thermal controls

While little empirical data exist to define transport characteristics within hot dome lavas, appropriate values may be estimated within a narrow range (Table 1) and provide the basis for any discussion on thermal infiltration constraints. Fractures 10–200 m long and over 50 m deep have been observed at 50–100 m spacing in the dome lavas at SHV following collapse events (Sparks et al., 2000). These are results of cooling as well as the presence of shears within the dome interior, allowing the loss of volatiles from the core. These fractures are regularly spaced at small scale (order of 20 m) and irregularly spaced at larger scale (order of 50 m) (Watts et al., 2002), and provide potential pathways for gas exfiltration and water infiltration. For an idealized dome segment with fracture spacing, s, (Fig. 1b) liquid depth penetration may be estimated by equating the quenching

Table 1
Summarized properties of the Soufrière Hills volcano dome rocks and associated fluids

Parameter	Description	Value
Solid Dome		
κ_R	Thermal diffusivity	1.4×10^{-6} m^2/s
c_R	Heat capacity	918 J/kg K
ρ_R	Density	2600 kg/m^3
C	Cohesive strength	0.1–0.5 MPa
α	Slope inclination	35–40°
ϕ	Friction angle	25°
s	Fracture spacing	1–100 m
T	Lobe temperature	400–800 °C
Magma		
ρ_M	Density	1300 kg/m^3
c_M	Heat capacity	1100 J/kg K
Water		
L_W	Latent heat of vaporization	2.5×10^6 J/kg
c_W	Heat capacity	4187 J/kg K
ρ_W	Density	1000 kg/m^3

potential (thermal flux) of rainfall, discharged from a tributary catchment area into a fracture, with the thermal flux conducted across the fracture wall as the penetrating water chills the margin to below boiling. In this first order analysis, we consider lateral heat flow to the fracture, which is cooled by rainfall entering the fracture. The anticipated effects of this infiltrating rainfall on the reduction of volume and pressure of interior gases is ignored, as the effect is likely small due to the large volume of gas present, and the large outward gas flux (SO_2 flux of 400 tonnes/day (Norton et al., 2002), and 25,000 tonnes/day of steam (Hammouya et al., 1998)). It is assumed that previous deluges and continuous contact with the atmosphere have sufficiently cooled the dome surface so that rainfall of intensity, i, reaches the fracture without evaporation. The thermal energy supplied by this fluid is applied as a constant thermal flux (F_R) at one end of a one-dimensional conductive heat-flow system, with an insulated boundary applied at the other end, representing the mid-point between adjacent fractures (Fig. 1b). We evaluate the drop in temperature at the fracture surface (ΔT_R) which results from the uniform heat flux (F_R), applied over the fracture surface over the duration of the deluge of dimensionless time, t_D. This defines the average required heat flux, F_R, at the fracture surface in a thermally conductive system (Carslaw and Jaeger, 1959 (Eq. (3.8.3)), p112) as

$$F_R = \frac{1}{l}\frac{\lambda_R \Delta T_R}{t_D + f(t_D)}, \tag{1}$$

where λ_R is the thermal conductivity of the rock and t_D is a non-dimensional time, defined by the thermal diffusivity of the rock, κ_R, length of the transfer segment, $l=s/2$, for fracture spacing, s, and the duration of the rainfall event, t, as $t_D=\kappa_R t/l^2$. The conductive function may be represented for cooling at the fracture surface and for the same boundary conditions as above (Carslaw and Jaeger, 1959 (Eq. (3.8.3)), p112) as

$$f(t_D) = \frac{1}{3} - \frac{2}{\pi^2}\sum_{n=1}^{\infty}\frac{1}{n^2}e^{-t_D n^2 \pi^2}. \tag{2}$$

Energy transfer within the system is represented by the balance between the thermal energy necessary to cool the fracture surface by an amount, ΔT_R (i.e. initial temperature minus 100 °C) and the thermal energy required to raise water temperature to vaporization, ΔT_W (i.e. 100 °C minus ~20 °C). The heat flux supplied by the penetrating water, F_W, may be similarly defined as

$$F_W = i\rho_W(c_W \Delta T_W + L_W), \tag{3}$$

for rainfall intensity, i, and constants of density, ρ, heat capacity, c, and latent heat, L. For a plane section of unit width, w, the energy balance between the heat flux supplied by the rainfall (F_W) falling over tributary area, l, is balanced by the heat flux from the fracture surface (F_R) distributed over the unknown water penetration depth, d. This is simply described as $w\ d\ F_R = w\ l\ F_W$, and we may solve for the unknown depth of penetration, d, by substituting from Eqs. (1) and (3) as,

$$4\frac{\kappa_R d}{is^2} = \frac{\rho_w(c_w \Delta T_W + L_W)}{\rho_R c_R \Delta T_R}[t_D + f(t_D)], \tag{4}$$

where the subscripts represent rock and water. We use this first-order approximation of behavior to represent the net thermal drawdown of temperatures at the fracture surface, for the prescribed quenching effect of the total rainfall amount. The model does not track spatial changes in temperature with depth along the fracture, nor the effects of time varying rainfall intensity or infiltration during the duration of the storm. Rather it represents the effect of a constant rainfall flux applied throughout the deluge event, and for the duration of that event.

Eq. (4) represents two limiting behaviors (Fig. 2). For (very) closely fractured media, thermal equilibrium is reached in the saturated surface concurrent with the rainfall (no horizontal thermal gradient is sustained). This occurs for $t_D \geq 10^0$, representing either events of significant duration (~1 year for a fracture spacing of 10 m) or closely spaced fractures (~3 days for a fracture

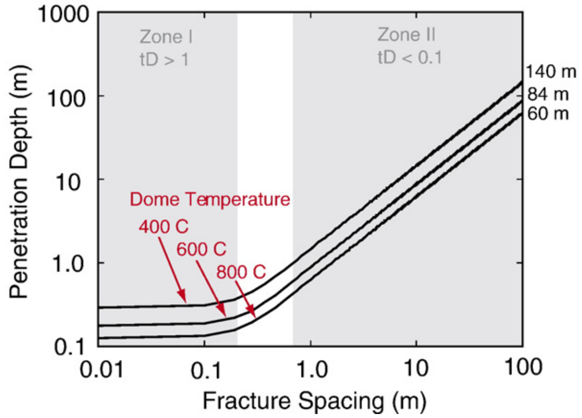

Fig. 2. Rainfall infiltration depths as a function of initial dome temperature. Note the development of two behaviors characteristic of short time (t_D) and long time. Cases of practical interest for Soufrière Hills relate to Zone II, for a typical fracture spacing of 50–100 meters and storm duration of 3 h with intensity of 25 mm/h.

spacing of 1 m), where the summation term of $f(t_D)$ in Eq. (4) is null, and depth penetration is defined as

$$d = \frac{\rho_w(c_w \Delta T_W + L_W)}{\rho_R c_R \Delta T_R}(t \times i). \tag{5}$$

This evolves naturally since the term in Eq. (4), $[t_D + f(t_D)] \rightarrow [t_D]$, and the depth of quenching is linearly dependent on rainfall duration, and independent of fracture spacing. This is because fractures are sufficiently closely spaced, such that at the depth of water penetration, everywhere the water and rock temperature are quenched to the same magnitude. For quenching from 800 °C, this represents a minimal depth of water penetration of about 1.5× the total rainfall amount, and for quenching from 200 °C, the penetration approximates 10× the rainfall amount (or 0.8 m for 75 mm in 3 h). This penetration will result in insignificant overpressures, only of the order of 10 kPa. This behavior is neither sufficient to promote failure, nor is it representative of SHV.

The second limiting behavior is for rainfall duration of $t_D \leq 10^{-2}$, which represents either shorter duration events (relative to thermal diffusivity) or more widely spaced fractures. This behavior is dominant for fracture spacing typical of Montserrat which, as discussed above, approximates 50–100 m. This again develops naturally from Eq. (4) where $[t_D + f(t_D)] \rightarrow [t_D + 1/3]$ but small t_D cannot merely be cancelled from Eq. (4) since, implicitly, it incorporates the effect of fracture spacing, $s = 2l$, also present within the relation. Depth penetration thus increases in direct proportion with spacing, and represents the case where the rainfall event chills the fracture margin, but does not significantly cool the interior. In this case, depth penetration can be approximated from Eq. (4) as

$$d \cong \frac{is^2}{4\kappa_R} \frac{\rho_w(c_w \Delta T_W + L_W)}{\rho_R c_R \Delta T_R}\left[1.13\sqrt{t_D}\right]. \tag{6}$$

This is the behavior of interest in promoting a collapse that may develop concurrently with the rainfall event. If the collapse is significantly delayed, remnant heat will remove the penetrating water.

From Fig. 2, possible depth penetrations are on the order of 3 to 60 m for the hottest case of an 800 °C dome, subject to 25 mm/hr intensity for 3 h, for fracture separations of 5 to 100 m. If the dome has been cooled by multiple prior events, depth penetration to 84 m is feasible at 600 °C and 140 m at 400 °C, each for the most widely spaced fractures (100 m). Occluding the most widely spaced and most deeply penetrating fractures will result in the greatest buildup in gas pressures — as these fractures will be the principal conduits for escaping gas.

Dominant fractures will develop as a natural consequence of the repeated quenching by storms (Nemat-Nasser et al., 1978) — more open fractures capture more water, propagate deeper than their neighbors, subsequently rob their neighbors of more water, and consequently further extend. This feedback favors the development of a few dominant fractures, rather than a field of multiple small fractures, enhancing water transport into the dome core.

4. Thermal evolution of the dome

With dome instability linked to the propensity for rainfall to infiltrate to thermally controlled depths, reasonable values for dome temperature must be established. Each successive deluge will progressively cool the existing dome and allow deeper infiltration from a subsequent storm. The rate of cooling within the dome rocks from a single precipitation event can be determined by equating the quenching thermal flux delivered by the infiltrating rainfall with the thermal mass of the dome. Recasting Eq. (5) for an effective height, h, of the active dome yields

$$\Delta T_R = \frac{\rho_w(c_w \Delta T_W + L_W)}{\rho_R c_R h}(t \times i), \tag{7}$$

which represents the attainment of thermal equilibrium between the dome mass and contacting rainwater ($t_D = \kappa_R t / h^2 \geq 1$). This defines average temperature change within the dome mass, and complements the local temperature change driven by fluid infiltration along fractures. These are not applied additively. Rainfall infiltration depth is first evaluated from local infiltration (Fig. 1b) by using Eq. (4), then the average dome temperature is updated from Eq. (7), using the same rainfall event.

4.1. Climatic air cooling

For any extended period of observation, air cooling of the dome should also be considered, and can generally be assumed additive to other cooling effects. We assume transfer to again be conductive-only and one-dimensional through a homogeneous solid dome. The upper boundary is constrained with a constant temperature boundary condition set to the ambient air temperature, with an insulated base, and with initial temperature within the solid set to T_o. This allows the average final temperature within the dome, T_{av}, (Carslaw and Jaeger, 1959, p97) to be evaluated as

$$T_{av} = \frac{8T_o}{\pi^2}\sum_{n=0}^{\infty}\frac{1}{(2n+1)^2}e^{-t_D(2n+1)^2\pi^2/4}, \qquad (8)$$

for the diffusive time $t_D = \kappa t/h^2$, where κ is the thermal diffusivity of the cooling rock, h is the thickness of the cooling dome, and t is the time since the initial temperature was established. The diffusive time required for average cooling by 50% (t_{50}) is 0.2, as obtained from plotting the diffusive series, Eq. (8), versus its characteristic time, t_D. Linearizing this as an average cooling rate for an 800 °C dome of 150 m radius (translatable to dome height, h, through hemispherical geometry) yields an average cooling rate of ~12 °C/year, excluding the effects of heat input, discussed below. This average rate reflects the cooling over the depth of the failing block comprising the edifice (~100 m), and yields a cooling rate considerably lower than that due to convective cooling of the near surface rocks. The convective near-surface heat flux evaluated for Soufriere Hills volcano is of the order of 4000 W/m^2 (Matthews and Barclay, 2004), compared to about 40 W/m^2 by conduction. This latter magnitude is controlled by the diffusive length for heat flow, which, for the block-interior, is large (~100 m).

4.2. Magma extrusion and heat influx

Heat loss due to local and global quenching, and as a result of air cooling, is countered by heat supply by magma infusion into, and gas loss from, the volcanic pile. The gain in thermal energy may be equated with the magmatic heat supply, assuming full thermal mixing within the dome rocks. Thus temperature increase within the dome may be defined as $\rho_M c_M(\varepsilon \cdot t)\Delta T_M = \rho_R c_R V_R \Delta T_R$ where the subscripts R and M represent the dome and magma, respectively, ε is extrusion rate, and all other parameters are as previously defined. The effect of gas loss is ignored. The mass of gas lost, at a peak near ~25,000 tonnes/day, is about two orders of magnitude lower than the mass gain from magma injection to the dome — at 5 m^3/s, this is about 10^6 m^3/day.

5. Stability model

With the rainfall-related controls on thermal evolution of the dome established, the influence of trapped gas overpressures on stability may be directly evaluated. The limit equilibrium stability of the phase II dome (November 1999 to present) is examined for anticipated magnitudes of gas overpressures. The resulting composite model focuses on the second eruptive phase, which includes two collapses of primary interest for rainfall induced failure: March 2000 and July 2001.

5.1. Morphology of the Soufriére Hills Volcano

Following an extended hiatus of residual activity, characterized by almost no fresh lava extrusion, subsequent to the 26 December 1997 eruption (Norton et al., 2002), new dome growth, termed the N99 Dome (Fig. 3), was observed in mid to late November 1999 (Carn et al., 2004). The growth occurred among the remnants of a large scar left by the explosions and collapses of the residual period (Norton et al., 2002), and was characterized as the second eruptive phase of the SHV since activity began in 1995. While the andesitic extrusion had switched intermittently between the NW, SW, and E sectors of the SHV (see Fig. 1 of Carn et al. (2004)), most of the growth had occurred in the eastern lobe (Carn et al., 2004), directed towards the Tar River Valley, and it was this growth that provided the basis for the 20 March 2000 and 29 July 2001 collapses.

Observed major collapses in 2000 and 2001 (~28 and $\sim 4510^{6}$ m^3) (Carn et al., 2004), several smaller events in June 2001, December 2001, July 2002, September 2002, and October 2002, all with volumes less than 5×10^6 m^3 (MVO (unpublished data, 2002)), and intermittent dome volume measurements using photogrammetric techniques (Carn et al., 2004), provide the basis for interpolation of extrusion rates presented in Table 2. Volumes reported in Table 2 describe the active portion of dome growth, exclude any residual mass previous to November 1999, and accommodate volumes

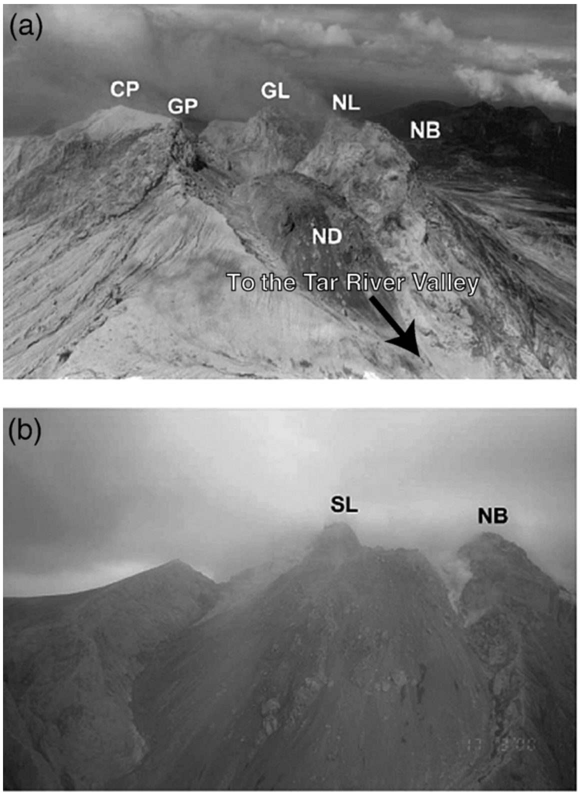

Fig. 3. (Carn et al., 2004) (a) Image of the young N99 dome on 16 December 1999, growing in an easterly direction towards the Tar River Valley. Remaining lobes from eruptive phase I are provided for reference (Chances Peak (CP), Galway's Peak (GP), Gages Lobe (GL), Northern Lobe (NL), Northeast buttress (NB)). (b) Advanced dome evolution on 17 March 2000. Rain triggered collapse of this dome on 20 March 2000; dome was replaced by another lava dome that collapsed on 29–30 July 2001. Crater spans ~1 km at rim.

lost by collapse in the events of March 2000 and July 2001 (Fig. 4).

5.2. Evolving dome geometry

Extrusion rates and dome volumes may be used to define the evolution of the dome. For an assumed hemispherical geometry, a time dependent radial footprint for the N99 dome (Fig. 5) may be defined. From the evolving dome volume, the idealized radial footprint is defined as $r=(6V/4\pi)^{1/3}$. From this hemisphere, a failing prismatic block is prescribed, with a cross-sectional area equal to that of the downslope quadrant of the hemisphere above the failure plane, as shown in Fig. 6. For a slope inclination, á, and dome radius, r, this equivalent height, h, is evaluated by equating the area of the two geometries — one prismatic and one the failing portion of a quarter circle of radius, r. In this, the areas of the spherical, A_S, and equivalent prismatic, A_B, blocks (see Figs. 6 and 1c) are defined as

$$A_S = \int_{\alpha}^{\pi/2}\int_0^r r dr d\theta - 1/2\sin(\alpha)\cos(\alpha) = \frac{r^2}{2}\left[(\pi/2-\alpha)-\sin(\alpha)\cos(\alpha)\right] \tag{9}$$

and $A_B = hr\cos(\alpha)$. Where $A_S = A_B$ we obtain

$$h = \frac{r(\pi/2-\alpha)}{2\cos(\alpha)} - \frac{r\sin(\alpha)}{2}, \tag{10}$$

where α is in radians, h represents the average height of the equivalent block (averaged between x_i and x_f in Fig. 6), and θ represents the area integrand from slope angle, α, to the opposing vertical at $\pi/2$. Unpublished data from MVO places the talus slope angle, α, at 33° in late 2002, setting an appropriate guideline for our model. Utilizing this talus slope angle and the extrusion rates presented in Table 1, the average height fluctuates between 0 and 114 m from November 1999 to October 2002. Importantly, block weights used in the above progression are not intended to be applied as weights in the stability calculation, as the failure block to be utilized (Fig. 7) will be partitioned by fracture spacing, s, not the full length of the hemispherical segment.

5.3. Destabilizing forces

For both effusive and non-effusive dome environments, the maximum gas overpressures resulting from

Table 2
Interpolated extrusion rates for the second eruptive phase of the N99 Soufrière Hills Volcano Dome

Extrusion phase	Period	Ending measured active (volume[a], Mm^3)	Interpolated extrusion rate, (m^3/s)
Phase I	1 Nov 99–14 Jan 00	15	2.4
Phase II	15 Jan 00–3 Mar 00	29	3.8
Phase III	4 Mar 00–8 Dec 00	64	2.9
Phase IV	9 Dec 00–2 Mar 01	–	2.6
Phase V	3 Mar 01–18 May 01	–	0[b]
Phase VI	19 May 01–23 Sept 01	12	2.6
Phase VII	24 Sept 01–27 Feb 02	38	2.7
Phase VIII	28 Feb 02–4 May 03	40–45	0.9

[a] Volume data compiled from Carn et al., 2004 and MVO (unpublished data, 2002).

[b] No dome growth observed over this period [MVO (unpublished data, 2002)].

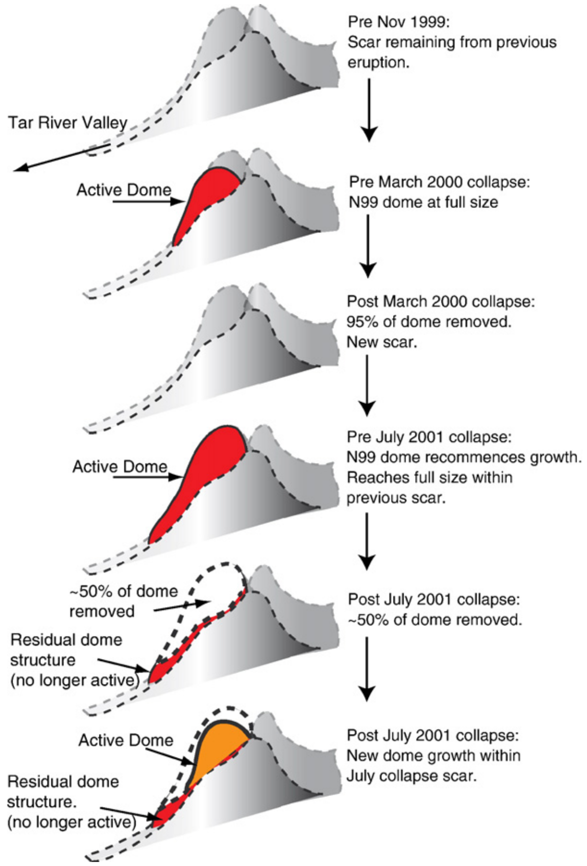

Fig. 4. Sequence of N99 dome activity through much of the current eruptive phase. Only the active dome portion (indicated in the figure) is included in the morphology of the stability model.

staunched gas flow are set by the infiltration depth, d, at $\rho_W \mathbf{g} d$ (Fig. 7), as the gas-entry or fluid-displacement pressure contribution was previously shown to be insignificant. This defines the destabilizing forces that may evolve on the unstable segment of an idealized dome flank. The isolated block may fail when the pressure-augmented destabilizing forces exceed the pressure-sensitive reduction in strength of the underlying inclined detachment. Instability is indexed by the "factor of safety", representing the ratio of stabilizing to destabilizing forces. A factor of safety of unity implies that the selected collapse geometry is at incipient failure.

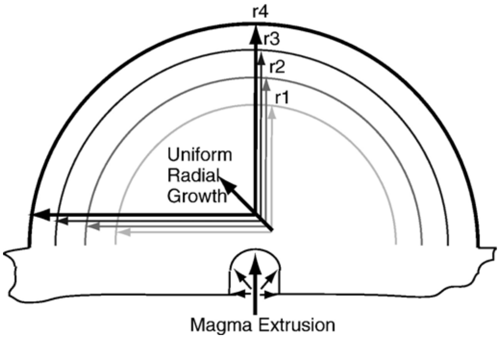

Fig. 5. Idealized time dependent radial dome footprint as a function of lava extrusion rate, for an idealized hemisphere.

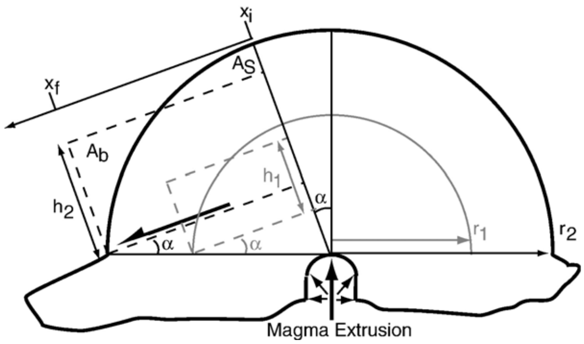

Fig. 6. Idealized representation of growth of the failing block, transitioning with increasing radial footprint. From r_1 to r_2, the block height, h, increases by a geometrically determined amount dependent on slope inclination, α, of the underlying talus and the radial increase. The new block height is averaged from x_i to x_f to produce an equivalent area (A_b) of the portion of the hemisphere (A_S) raised at the same angle and for the same length, x_i to x_f.

The geometry of Fig. 7 examines the lowermost portion of the disjointed dome portion of thickness, h, and inclination, α, isolated by fracture spacing, s, which cuts the full depth of the segment. Infiltrating rainwater, as controlled by the thermal and hydraulic mechanisms discussed above, creates a hydrostatic liquid pressure that sets the maximum value for capped, underlying vapor overpressures. This pressure can be represented as, $\gamma_W d\cos(\alpha)$, where γ_W is the unit weight of water ($\rho_W \mathbf{g}$), and d is liquid depth penetration. Equilibrium is established for this geometry as the ratio of the stabilizing forces modulated by cohesive strength, c, block weight, W, and friction angle, φ, to the destabilizing influence of the back-scarp water, F_W, and vapor, F_V, forces and by the vapor uplift force, F_U, applied to the basal plane. The factor of safety, F_s, can therefore be defined for a unit thickness of slope as,

$$F_s = \frac{cs + (W\cos(\alpha) - F_U)\tan(\varphi)}{W\sin(\alpha) + F_W + F_V} \tag{11}$$

where block weight $W = s \times h \times \gamma_R$, uplift force $F_U = 1/2d\cos(\alpha) \times \gamma_W \times s$, vaporized water force $F_V = d\cos(\alpha) \times \gamma_W \times (h-d)$, liquid water force $F_W = 1/2d^2 \times \cos(\alpha) \times \gamma_W$, where γ_R is the unit weight of the rock, and all other components are identified in the geometry of Fig. 7. Values of $F_s \leq 1$ imply failure.

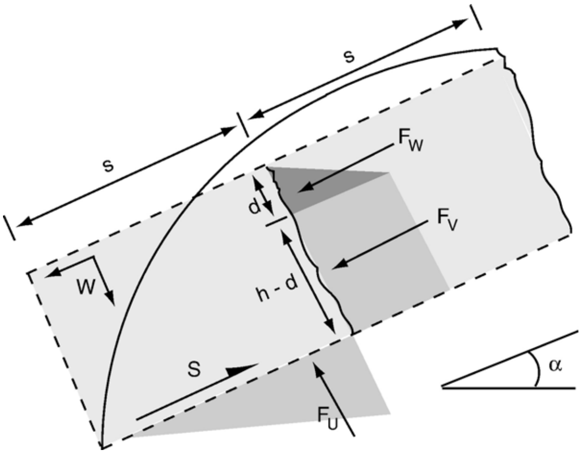

Fig. 7. Force balance on isolated dome block, separated by fracture spacing, *s*, and block height, *h*. From the block portion isolated by fracture spacing: Down-slope destabilizing forces of block weight, *W*, liquid water force, F_W, and vapor force, F_V, from vaporized water and/or interior pressures cumulatively capped by infiltration depth at $\rho_W gd$, are augmented by the vapor uplift force, F_U, and opposed by shear resistance, *S*, and the weight component normal to the failure plane raised at talus slope inclination, α.

5.4. Parametric constraints

Critical controlling parameters are the strength properties of the dome edifice that act along evolving plane of detachment, and the environmental factors of interior gas pressures. The strength properties of hot dome lava (~800 °C) have not been measured. However, expulsion of dome spines to 100 m height by interior pressures reckoned at 5 MPa, together with inverse calculations of stable hot edifices, yield combined cohesive strengths on the order 0.5 MPa and frictional strengths of 25°, but these are poorly constrained. The importance of these values is discussed elsewhere (Voight and Elsworth, 2000).

6. Model results

Considering the composite effects of all constraints discussed above, a unified model considers the daily evolution of the dome. Defined magma extrusion rates and rainfall records (total amount in one day) are used to track the evolving average temperature in the near-surface dome rocks. This average temperature constrains hydraulic depth penetration for a given deluge intensity. Infiltration dependent overpressures were then applied to the unstable segment of an idealized hemispherical dome (Fig. 7), and incremented for volume gain by infusion into the dome pile, or decremented for collapse (Fig. 6). Additional parameters incorporated into the model are presented in Table 3. Factor of safety, F_s, is then evaluated.

Applying parameters from Table 3 yields the evolution of factor of safety defined for the period 1 January, 2000 to 31 October, 2002, as evident in Fig. 8. Fig. 8a shows the response where changes in geometry with dome growth and then collapse are accommodated, and Fig. 8b where the geometry is retained constant. Using consistent parameters, the rainfall deluges of March 2000 and July 2001 are shown to bring the edifice close to failure for both events, but only where the dome geometry is incremented for magma influx (Fig. 8a). This is an important outcome, as without this morphological consideration, it is not possible to match observed behavior. While the heaviest rainfall episodes produced the deepest spikes in depth penetration and, subsequently, F_s, these occurrences did not necessarily reach below the required value of unity that implies incipient failure when the dome was experiencing a stage of renewal. However, relative to the large F_s immediately post failure (~3), the F_s approaches within a few percent of instability (F_s-1) around the time of failure. This discrepancy can clearly be accommodated by variability in strength and environmental parameters.

It is clear from the progression towards failure illustrated in Fig. 8 that random high intensity rainfall events are insufficient to trigger failure, if the thermal and mechanical conditions are insufficiently primed to allow failure. Where geometry is invariant, quenching by rainfall is insufficient alone to bring the dome to failure by a sufficiently deep penetration of rainfall. Rather, the dome must be primed for imminent failure by the evolving and steepening slope geometry. The destabilizing influence of rainfall is relatively minor, requiring that the slope is first primed for failure by oversteepening.

Next we consider seismic amplitude as a measure of dome activity. MVO seismic measurements have traditionally used real-time seismic amplitude measurement (RSAM), as described by Endo and Murray (1991), to yield a simple quantitative measure of overall seismicity. RSAM measures the average absolute amplitude of seismic signals, in units of “counts”, by using a

Table 3
Specific dome parameters utilized in the applied stability model

Parameter	Description	Value
C	Cohesive strength	0.5 Mpa
α	Slope inclination	33°
ϕ	Friction angle	25°
s	Fracture spacing	75 m
T	Lobe temperature	800 °C on 1 November, 1999

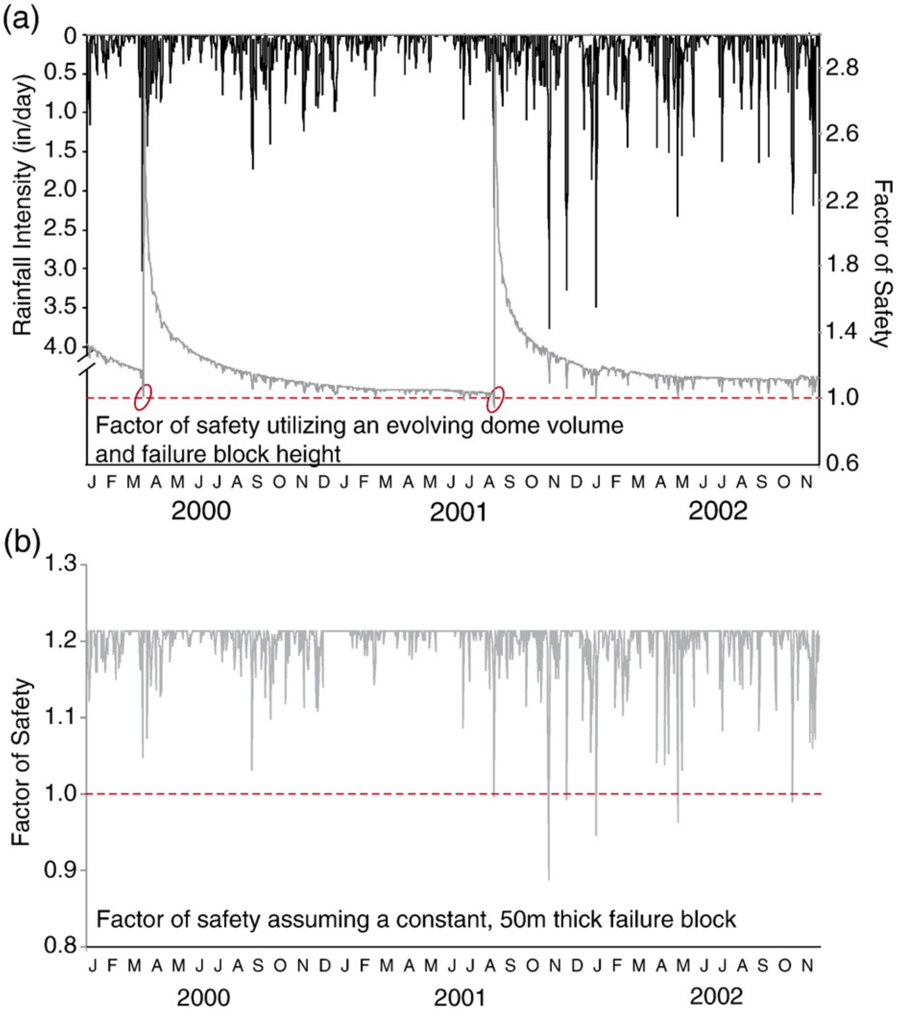

Fig. 8. Factor of safety (F_s) determination for the period January 1, 2000 to November 1, 2002. (a) Rainfall intensity (read top left axis) and F_s (read right axis), where F_s is a function of evolving lobe thickness. (b) F_s as a function of constant lobe thickness. Rainfall intensity recorded by University of East Anglia rain gauges at Hope (5 km northwest of dome).

sampling rate of about 60 samples per second. It does not discriminate between various event types, apart from spikes that can reflect pyroclastic flows, and the strength of signal depends on seismometer location. The primary drawback to this RSAM system is the lack of an appropriate calibration basis and the necessity of manually correcting the timestamp that is attached to the data.

The analog RSAM system was updated to a digital network, BSAM, on 20 March 2000 to improve accuracy. The new BSAM system again presents readouts in “counts”, but can be calibrated into meaningful seismic units which are transferable from one seismic event to another. Additionally, BSAM measurements are time stamped with a GPS system. Utilizing the BSAM system, seismic data can be converted into “reduced displacement”, a widely used metric for continuous volcano-seismic signals. Reduced displacement is expressed in units of cm^2 and can be compared from one volcano to another. The resulting values can, then, be corrected for distance from the seismic source and for attenuation. When this transferable amplitude is achieved, the signal can then be averaged across all digital stations near the source. The evolution of factor of safety with reduced displacement, averaged over one day and across all MVO digital stations, is shown in Fig. 9.

Notably, high amplitude seismic events do not always accompany collapse. Only relatively low amplitudes are present for the March 2000 collapse, although high rainfalls of September, October and December 2001 do elicit strong seismic signals. In all cases, these strong

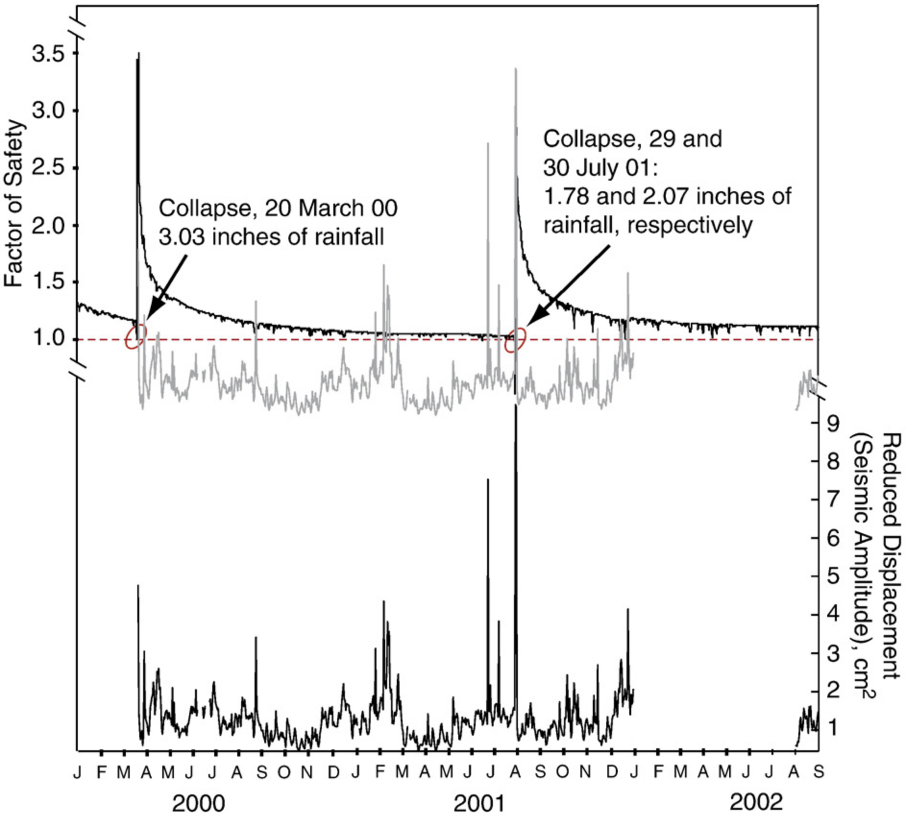

Fig. 9. Correlation of F_s to reduced displacement seismic amplitude for the period of 1 Jan 2000 to 1 Sept. 2002. Rainfall intensity recorded by University of East Anglia rain gauges at Hope (5 km northwest of dome). Reduced displacement is averaged over one day, corrected for station distance from the seismic source and attenuation, and is an average of BSAM data collected from Garibaldi Hill, St. Georges Hill, Long Ground, Roches Yard, South Soufrière Hills, and Windy Hill. Light gray seismic signal is a replication of the lowermost black signal, moved upward for closer comparison to factor of safety.

signals were triggered by total rainfall magnitudes of more than 3 in/day (75 mm/day). This suggests that BSAM may be a crude predictor of the effect of local rainfall intensities on stability, but the pre-existing state of dome pile (thermal and physical state and principally geometry) may exert the main control on impending failure. An event of only ~2 in/day was required to trigger the July 29 2001 collapse, by bringing a metastable dome to failure, whereas a more stable dome in March 2000 required a larger impetus (~3 in/day).

The short timescale triggers in developing failure may be examined for the near continuous rainfall history record available throughout the July 29–30 2001 collapse. When the same model is applied to this magnified window, the resulting histories of precipitation, reduced displacement, averaged over one minute, and factor of safety are shown in Fig. 10. The model maintains a general correlation between the reduction in F_s and the occurrence of clusters of seismic events, although the switch from one day averaged to near continuous time rainfall measurements alters the sensitivity of the analysis. At this scale, where tracking morphological changes becomes impossible, there is a difficulty in resolving the influence of individual rainfall events. At the time of the July 2001 high rainfall events, the dome was metastable, and a variety of rainfall events of varying intensities and durations could conceivably trigger failure. This ability appears beyond the resolution of the current model with a difficulty in resolving between various degrees of instability.

From Fig. 10, F_s falls below unity ~12 h prior to the 29 July 2001 collapse, with no impact on the seismic signal, while a more sustained drop in F_s, lasting several hours, precedes the collapse event by approximately 1 h and continues throughout the first collapse phase. The second collapse phase is marked by a shorter duration drop in F_s below unity, although inclusion of volume loss throughout the collapse event would negate this occurrence. In general, collapse timing does not coincide directly with the evaluated F_s, but instead is slightly delayed.

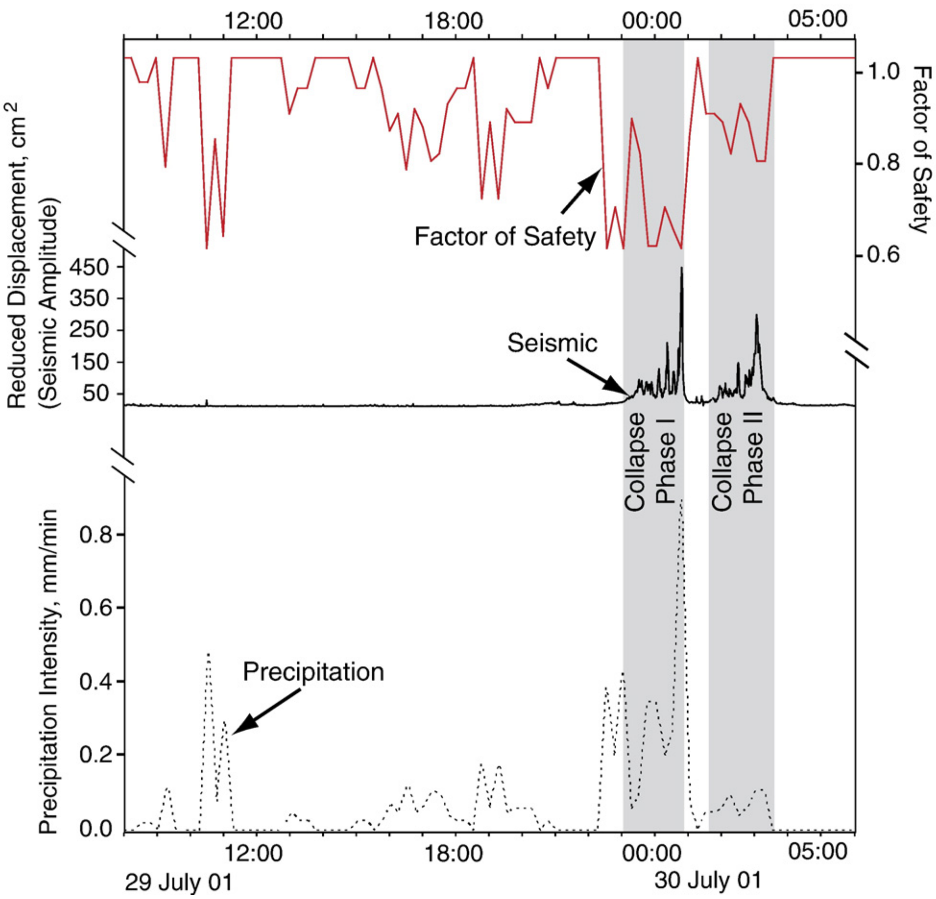

Fig. 10. Chronology of 29 July 2001 collapse. Rainfall (black dashed line, read on lower left axis) recorded at Hope. Reduced displacement (solid black line, read on top left axis) is averaged over all digital stations (see Fig. 10) with the signal averaged over one minute. Factor of safety (top solid line, read on right axis) falls below unity, and for several hours through the first eruptive phase, and dips only briefly below unity during the second phase. This brief dip correlates with the strongest seismic signal. Antecedent rainfall began at 08:00 with the heaviest occurring from 21:00 to midnight (07/30).

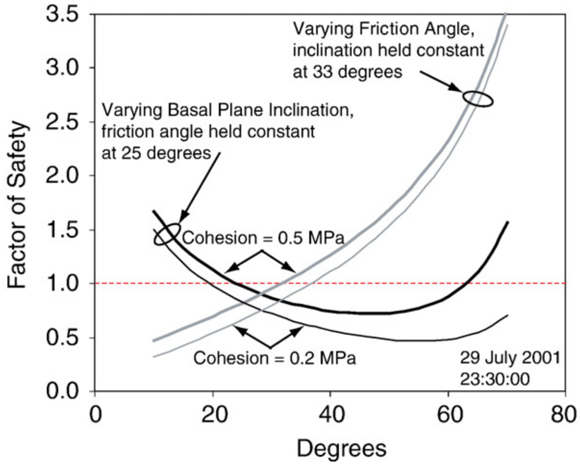

Fig. 11. Sensitivity analysis for factor of safety at an arbitrary time. Changes in F_s for varied friction angle with failure plane held constant, and for constant friction with varied inclination of the failure plane.

Beyond problems associated with the fine resolution of factors of safety in time, the relative sensitivity of the model to changes in individual parameters may be examined. Arbitrarily choosing a single time step from Fig. 10, a parameter sensitivity analysis illustrates how the model would have appeared at the chosen time should the values of Table 3 have been chosen differently (Fig. 11). The point of intersection between the 0.5 MPa curves represents the F_s value at 23:30:00 in Fig. 10. Consequently, further refinement of the model parameters may yield significant changes in failure prediction.

7. Conclusions

A thermal-hydrologic mechanism is proposed to control the rainfall-triggering of dome collapse. The model incorporates the influence of local quenching in fractures within the dome carapace that staunches gas flow and allows interior gas pressures to build. This model is linked with the evolution of mean dome-flank temperatures which are reduced both by the rainfall flux, and by climatic cooling. These mechanisms of cooling are countered by the supply of heat into the dome, delivered by the infusing magma. This both increases temperatures and overloads the slope, countering the restoring influence of cohesion. This model is applied to examine rainfall-concurrent collapses observed in the period January 2000 to December 2002, for which rainfall, reduced displacement seismic output, dome volume, and collapse timing records are available. The model is able to replicate, to reasonable accuracy, the collapse events that are observed, including the triggering of collapse by rainfall events. When the geometric evolution of the dome is neglected, the occurrence of collapses cannot be followed. Only when dome growth is accommodated can the timing of failures be correlated with rainfall events. The principal influence in driving the dome to failure is the evolving geometry in bringing the dome to a condition of metastability. This effect is more significant than the influence of the extreme rainfall events, which are similar in magnitude (~2–3 in/day) and more frequent than the major collapse events. The extreme rainfall events are able to trigger failure, but only when the dome flank is first primed for failure.

Acknowledgements

This work is a result of the support by the National Science Foundation under grants CMS-9908590, EAR-9909673, EAR-0116826, and EAR-04-08709. Generous support of colleagues at the Montserrat Volcano Observatory (MVO) is acknowledged, and we thank Jenni Barclay and Adrian Matthews, University of East Anglia, for permission to use rain-gauge data for Fig. 11. In addition, we are grateful for review comments and helpful suggestions from Jenni Barclay and Larry Mastin. These have ultimately produced a stronger and more cohesive document.

References

Abdurachman, E.K., Bourdier, J.L., Voight, B., 2000. Nuees ardentes of 22 November 1994 at Merapi Volcano, Java, Indonesia. Journal of Volcanology and Geothermal Research 100 (1–4), 345–361.

Calder, E.S., Luckett, R., Sparks, R.S.J., Voight, B., 2002. Mechanisms of lava dome instability and generation of rockfalls and pyroclastic flows at Soufriere Hills volcano, Montserrat. In: Druitt, T.H., Kokelaar, B.P. (Eds.), The Eruption of Soufrière Hills Volcano, Montserrat, from 1995 to 1999, vol. 21. Geological Society, London, Memoirs, pp. 173–190.

Carn, S.A., Watts, R.B., Thompson, G., Norton, G.E., 2004. Anatomy of a lava dome collapse: the 20 March 2000 event at Soufriere Hills Volcano Montserrat. Journal of Volcanology and Geothermal Research 31, 241–264.

Carslaw, H.S., Jaeger, J.C., 1959. Conduction of Heat in Solids, Second Edition. Oxford University Press. 510 pp.

Elsworth, D., Voight, B., 2001. The mechanics of harmonic gas-pressurization and failure of lava domes. Geophysical Journal International of the Royal Astronomical Society 145, 187–198.

Elsworth, D., Voight, B., Thompson, G., Young, S.R., 2004. Thermal-hydrologic mechanism for rainfall-triggered collapse of lava domes. Geology 32 (11), 969–972.

Fink, J.H., Griffiths, R.W., 1998. Morphology, eruption rates, and rheology of lava domes: Insights from laboratory models. Journal of Geophysical Research 103 (B1), 527–545.

Hammouya, G., Allard, P., Jean-Baptiste, P., Parello, F., Semet, M.P., Young, S.R., 1998. Pre-and syn-eruptive geochemistry of volcanic gases at Soufriere Hills of Montserrat, West Indies. Geophysical Research Letters 25 (19), 3685–3688.

Herd, R., Edmonds, M., Strutt, M., Ottermeiler, L., 2003. The collapse of the lava dome at Soufriere Hills Volcano, 12–15 July 2003. Eos (Transactions, American Geophysical Union) 84 (46), F1596.

Leverett, M.C., 1941. Capillary behavior in porous solids. AIME Transactions 142–152.

Lide, D.R. (Ed.), 2003. CRC Handbook of Chemistry and Physics, 84th ed. CRC Press, Boca Raton, Florida.

Mastin, L., 1994. Explosive tephra emissions at Mount St. Helens, 1989–1991 — The violent escape of magmatic gas following storms. Bulletin of the Geological Society of America 106, 175–185.

Matthews, A.J., Barclay, J., 2004. A thermodynamical model for rainfall-triggered volcanic dome collapse. Geophysical Research Letters 31 (5), L05614. doi:10.1029/2003GL019310.

Matthews, A., Barclay, J., Carn, S., Thompson, G., Alexander, J., Herd, R., Williams, C., 2002. Rainfall-induced volcanic activity on Montserrat. Geophysical Research Letters 29 (0, 10), 1029.

Miller, T.P., 1994. Dome growth and destruction during the 1989–1990 eruption of Redoubt Volcano. Journal of Volcanology and Geothermal Research 26 (1–4), 197–212.

Miller, A.D., Stewart, R.C., White, R.A., Luckett, R.L., Baptie, B.J., Aspinall, W.P., Latchman, J.L., Lynch, L.L., Voight, B.V., 1998. Seismicity associated with dome growth and collapse at the Soufriere Hills volcano, Montserrat. Geophysical Research Letters 25 (18), 3401–3404.

Nakada, S., Fujii, T., 1993. Preliminary report on the activity at Unzen Volcano (Japan). November 1990–November 1991: dacite lava domes and pyroclastic flows. Journal of Volcanology and Geothermal Research 54, 319–333.

Nemat-Nasser, S., Keer, L., Parihar, K., 1978. Unstable growth of thermally induced interacting cracks in brittle solids. International Journal of Solids and Structures 14, 409–430.

Norton, G.E., Watts, R.B., Voight, B., Mattioli, G.S., Herd, R.A., Young, S.R., Devine, J.D., Aspinall, W.P., Bonadonna, C., Baptie, B.J., Edmonds, M., Harford, C.L., Jolly, A.D., Loughlin, S.C., Luckett, R., Sparks, R.S., 2002. Pyroclastic flow and explosive activity of the lava dome of Soufrière Hills volcano, Montserrat, during a period of virtually no magma extrusion (March 1998–November 1999). In: Druitt, T.H., Kokelaar, B.P. (Eds.), The Eruption of Soufrière Hills Volcano, Montserrat, from 1995 to 1999. Memoirs, vol. 21. Geological Society, London, pp. 467–481.

Ouyang, Z., Elsworth, D., 1993. Evaluation of groundwater flow into mined panels. Int. J. R. Mechs. Min. Sci. and Geomechs. Abstr., vol. 30, no. 2, pp. 71–80.

Simmons, J., Elsworth, D., Voight, B., 2003. Instability of exogenous lava lobes during intense rainfall. Bulletin of Volcanology 66 (8), 725–734.

Sparks, R.S.J., et al., 1998. Magam production and growth of the lava dome of the Soufriere Hills volcano, Montserrat, West Indies: November 1995 to December 1997. Geophysical Research Letters 25 (18), 3421–3424.

Sparks, R.S.J., Murphy, M.D., Lejeune, A.M., Watts, R.B., Barclay, J., Young, S.R., 2000. Control on the emplacement of the andesite lava dome of the Soufriere Hills volcano, Montserrat by degassing-induced crystallization. Terra Nova 12, 14–20.

Voight, B., Elsworth, D., 2000. Instability and collapse of lava domes. Geophysical Research Letters 27 (1), 1–4.

Voight, B., Constantine, E.K., Siswowidjoyo, S., Torley, R., 2000. Historical eruptions of Merapi Volcano, Central Java, Indonesia, 1768–1998. Journal of Volcanology and Geothermal Research 100, 69–138.

Watson, I.M., Oppenheimer, C., Voight, B., Francis, P.W., Clarke, A., Stix, John, Miller, A., Pyle, D.M., Burton, M.R., Young, S.R., Norton, G., Loughlin, S., Darroux, B., 2000. The relationship between degassing and ground deformation at Soufriere Hills Volcano, Montserrat. Journal of Volcanology and Geothermal Research 98 (1–4), 117–126.

Watts, R.B., Herd, R.A., Sparks, R.S.J., Young, S.R., 2002. Growth patterns and emplacement of the andesite dome at Soufriere Hills volcano, Montserrat. In: Druitt, T.H., Kokelaar, B.P. (Eds.), The Eruption of Soufrière Hills Volcano, Montserrat, from 1995 to 1999. Memoirs, vol. 21. Geological Society, London, pp. 115–152.

Widiwijayanti, C., Clarke, A., Elsworth, D., Voight, B., 2005. Geodetic constraints on the shallow magma system at Soufrière Hills volcano, Montserrat. Geophysical Research Letters 32, L11309. doi:10.1029/2005GL022846.

Yamasato, H., Kitagawa, S., Komiya, M., 1998. Effect of rainfall on dacitic lava dome collapse at Unzen volcano, Japan. Papers in Meteorology and Geophysics 48 (3), 73–78.